Princeton Plasma Physics Laboratory

PPPL- 4332

PPPL- 4332

ASSESSMENT OF AN OBLIQUE ECE DIAGNOSTIC FOR ITER

Gary Taylor and Robert W. Harvey

July 2008

Prepared for the U.S. Department of Energy under Contract DE-AC02-76CH03073.

Princeton Plasma Physics Laboratory
Report Disclaimers

Full Legal Disclaimer

Trademark Disclaimer

PPPL Report Availability

Princeton Plasma Physics Laboratory:

http://www.pppl.gov/techreports.cfm

Office of Scientific and Technical Information (OSTI):

http://www.osti.gov/bridge

Related Links:

U.S. Department of Energy

Office of Scientific and Technical Information

Fusion Links

ASSESSMENT OF AN OBLIQUE ECE DIAGNOSTIC FOR ITER

Gary Taylor

Princeton Plasma Physics Laboratory, Princeton, NJ 08543, USA

Robert W. Harvey

CompX, Del Mar, CA 92014, USA

Abstract

A systematic disagreement between the electron temperature measured by electron cyclotron emission (T_{ECE}) and laser Thomson scattering (T_{TS}), that increases with T_{ECE}, is observed in JET and TFTR plasmas, such that $T_{ECE} \sim 1.2\ T_{TS}$ when $T_{ECE} \sim 10$ keV. The disagreement is consistent with a non-Maxwellian distortion in the bulk electron momentum distribution. ITER is projected to operate with $T_e(0) \sim$ 20-40 keV so the disagreement between T_{ECE} and T_{TS} could be > 50%, with significant physics implications. The GENRAY ray tracing code predicts that a two-view ECE system, with perpendicular and moderately oblique viewing antennas, would be sufficient to reconstruct a two-temperature bulk distribution. If the electron momentum distribution remains Maxwellian the moderately oblique view could still be used to measure $T_e(R)$. A viewing dump will not be required for the oblique view and plasma refraction will be minimal. The oblique view has a similar radial resolution to the perpendicular view, but with some reduction in radial coverage. Oblique viewing angles of up to 20^o can be implemented without a major revision to the front end of the existing ITER ECE diagnostic design.

I. INTRODUCTION

In optically thick magnetically-confined tokamak plasmas where $T_e \leq 7$ keV, the electron temperature measured by ECE, T_{ECE}, is generally in good agreement with the electron temperature measured by laser Thomson scattering, T_{TS}, with any differences being less than 10%. However, there has been growing evidence that this may not be true in tokamak plasmas at higher T_e, at least under some conditions. Measurements of T_{ECE} significantly greater than T_{TS} were first reported in optically thick TFTR plasmas when $T_{ECE} > 7$ keV [1,2]. The difference between T_{ECE} and T_{TS} became larger with increasing T_{ECE}. Later a similar phenomenon was reported for JET plasmas [3]. An analysis of the JET ECE data suggested that in regions of the plasma where $T_e \geq 7$ keV there may be a non-Maxwellian distortion in the bulk electron velocity distribution at velocities in the vicinity of the average thermal velocity. Similar behavior has also been reported during ECRH plasmas in the FTU tokamak [4].

Figure 1 shows an example of the discrepancy between $T_{ECE}(0)$ and $T_{TS}(0)$ observed on TFTR. The disagreement between T_{ECE} and T_{TS} reaches about 20% at 10 keV. A similar discrepancy is measured on JET [3]. Modeling of the JET ECE data shows that the discrepancy can be explained as resulting from a distortion of the electron momentum distribution from Maxwellian in the range $0.75u_{th} \leq u \leq 1.5u_{th}$, where u_{th} is the average electron thermal momentum. To date, no physical mechanism has been proposed that can explain how the bulk electron velocity distribution can become non-Maxwellian in the vicinity of the average thermal momentum. Unless there is a strong driving mechanism, such as a resonant wave-particle interaction that can modify the electron phase space, electron-electron collisions in the bulk will keep the bulk of the electron momentum

distribution Maxwellian. Extrapolating the observations on TFTR and JET to ITER plasmas parameters, where $T_e(0)$ is expected to be 20-40 keV, the disagreement between T_{ECE} and T_{TS} may be significant, perhaps as large as 50% and if the bulk electron momentum distribution becomes non-Maxwellian there could be significant physics implications. On ITER, it will be useful to have the ability to measure T_{ECE} from distinct electron energy ranges.

An obliquely-viewing ECE diagnostic has been installed on JET to simultaneously measure the T_{ECE} at ~0^o, ~10^o and ~20^o with respect to perpendicular to the magnetic field, in order to study the behavior of the bulk electron distribution at high T_e [5-7]. A similar oblique ECE view has been considered for the proposed ITER midplane ECE diagnostic [8] at equatorial port E9. The current design for the ITER ECE diagnostic includes two perpendicular viewing antennas. This assessment study looked at the viability of a moderately oblique ($\leq 20^o$ from perpendicular) ECE antenna at port plug E9, including consideration of design constraints imposed by the existing port plug architecture and the potential measurement capability for typical ITER plasma scenarios. This study answers the following questions:

(a) What range of electron energies would a moderately oblique antenna be sensitive to at 10^o and 20^o to perpendicular?

(b) Can the moderately oblique view be used for T_e measurements if the plasma electron distribution remains Maxwellian at high T_e?

(c) If the electron energy distribution has a bulk distortion, can a two-temperature distribution be reconstructed with only two views, one perpendicular and one moderately oblique?

The study also looked at options for providing a moderately oblique view at ITER equatorial port E9. Section II of this report summarizes the modeling results, section III discusses a possible implementation of an oblique view at equatorial port E9 and section IV presents conclusions and recommendations from this assessment study.

II. MODELING RESULTS

The ECE modeling for this assessment study was performed with the GENRAY 3-D ray tracing numerical code [9]. GENRAY is an all frequencies ray tracing code that calculates ECE from thermal and non-thermal distributions. Emission and absorption coefficients are calculated at each point along rays originating at the ECE antenna, and the radiation transport equation is solved back to the antenna, as described in Ref. [10]. The ray trajectories are calculated using either cold or hot plasma dispersion relations, along with a numerical, fully relativistic emission and absorption calculation for thermal or non-thermal distribution functions.

ECE modeling was performed for two ITER plasma scenarios; an H-mode plasma with 30 MW of neutral beam heating and 20 MW of ion cyclotron resonance heating, and a plasma with 30 MW of lower hybrid current drive, providing off axis plasma current at a normalized minor radius (r/a) = 0.65. For most of the ECE modeling calculations a single ray was used, instead of a bundle of rays filling the antenna pattern. The effect of adding a finite antenna pattern width on the model results will be discussed later in this section, but in general it had a relatively minimal effect on radial resolution. Most of the numerical modeling was performed using non-relativistic ray tracing. However, in the few sample cases where relativistic ray tracing was used no significant difference in ray trajectory could be seen compared to the non-relativistic calculation.

The modeling results are summarized below and have been employed to answer the three questions posed in the introduction.

(a) ***What range of electron energies would a moderately oblique antenna be sensitive to at 10^o and 20^o to perpendicular?***

Figure 2 shows the input parameters used for the H-mode plasma modeling. The electron density profile (Fig. 2(a)) for this case is flat over most of the profile with a central density of 1 x 10^{20} m^{-3} and the electron temperature profile (Fig. 2(b)) is peaked with a temperature on axis of 25 keV. The poloidal cross section of the magnetic equilibrium is shown in Fig. 2(c). The position of the ECE antenna, shown schematically, lies close to the midplane of the plasma. ECE was modeled for a plasma with a Maxwellian electron velocity distribution (blue solid line in Fig. 2(d)) and a "two-temperature" non-Maxwellian distribution (red dashed line in Fig. 2(d)) that has the effective temperature of the electron velocity distribution between 0.75 and 1.5 times the electron thermal momentum increased by a factor of two.

Figure 3 shows ECE spectra simulated by GENRAY. T_{ECE} is plotted versus the emission frequency normalized to the fundamental electron cyclotron frequency on axis, $f/f_{ce}(0)$, where $f_{ce}(0)$ = 149 GHz. The O-mode ECE spectra for the H-mode case are shown in Fig. 3(a). The ECE spectra for the Maxwellian electron distribution are indicated by the three solid blue lines, the thickest line being for the perpendicular view and the thinnest being for the view that is 20^o from perpendicular. The geometry of the views is illustrated schematically in Fig. 3(c). The emission frequency range covers the fundamental, second and third harmonic ECE resonances in the plasma. For the H-mode

plasma conditions it is possible to use fundamental O-mode ECE to measure $T_e(R)$ well beyond the plasma axis using the perpendicular and oblique views. All three fundamental O-mode spectra show $T_{rad}(0)$ = 25 keV. The ECE spectra for the two-temperature non-Maxwellian electron distribution, shown in Fig. 2(d), are indicated by the three dashed red lines, the thickest line being for the perpendicular view and the thinnest being for the view that is 20^o from perpendicular. For the perpendicular and 10^o oblique views $T_{rad}(0)$ = 40 keV, for the 20^o oblique view $T_{rad}(0)$ = 25 keV, the same as for the Maxwellian plasma. The 20^o oblique view ECE spectrum is very similar to the spectrum for the Maxwellian. The X-mode ECE spectra for the H-mode case are shown in Fig. 3(b). The second harmonic X-mode cannot be used to measure $T_e(R)$ all the way into the plasma axis, because of third harmonic absorption. The perpendicular and 10^o oblique views can be used to measure $T_e(R)$ into about r/a=0.2 on the low field side of the axis. The 20^o oblique view can only be used to measure $T_e(R)$ into about r/a=0.4. The perpendicular and 10^o oblique views are sensitive to the non-Maxwellian distortion in the bulk electron distribution at second and particularly at third harmonic. The 20^o oblique view is insensitive to the bulk distortion.

Figure 4 shows the range of electron energies that contribute to the measured O-mode ECE from the H-mode plasma. This is the specific intensity of the radiation at each frequency, per unit energy range of the emitting electrons. Figures 4(a), 4(c) and 4(e) show the energies contributing to the measured flux when the electron velocity distribution is Maxwellian. Figs. 4(b), 4(d) and 4(f) show the energies contributing to the measured flux when the electron velocity distribution has a two-temperature non-Maxwellian bulk. For each of the three ECE antenna orientations the energies

contributing to the measured ECE are similar for the Maxwellian and non-Maxwellian electron distribution. For the perpendicular view (Fig. 4(a) and (b)) the electrons contributing to the measured ECE have energies in the range 0-10 keV at fundamental increasing to 40-70 keV at third harmonic. For the 10^o oblique view (Fig. 4(c) and (d)) the electrons contributing to the measured ECE have energies in the range 10-25 keV at fundamental increasing to 30-60 keV at third harmonic. For the 20^o oblique view (Fig. 4(e) and (f)) the electrons contributing to the measured ECE have energies in the range 30-80 keV at fundamental increasing to 30-140 keV at third harmonic.

Figure 5 shows the range of electron energies that contribute to the measured X-mode ECE from the H-mode plasma. The trends of viewing higher electron energies at higher harmonics and more oblique angles are similar to the O-mode polarization results. However, the electron energies to which the ECE is sensitive are about half as high as for the O-mode polarization. Also, the range of energies contributing to emission at a given angle and harmonic are much narrower than for O-mode polarization.

Figure 6 and 7 show enlarged views of the emission flux spectra for fundamental O-mode and second harmonic X-mode emission measured at the edge of the plasma, for the H-mode plasma with a Maxwellian and Non-Maxwellian bulk, respectively. The perpendicular view is sensitive to electrons with kinetic energies below 10 keV, the 10^o oblique view is sensitive to electrons with kinetic energies in the range 5-20 keV and the 20^o view is sensitive to electrons with kinetic energies in the range 30-80 keV.

In summary, the perpendicular viewing antenna will be sensitive to electron kinetic energies of less than 10 keV, the 10^o oblique view will be sensitive to energies in the

range 5-20 keV and the 20^o oblique view will be sensitive to energies in the range 20-70 keV.

(b) Can the moderately oblique view be used for T_e measurements if the plasma electron distribution remains Maxwellian at high T_e?

Figure 8 shows a plot of the specific ECE intensity per unit distance along the ray, in O-mode polarization, received at the edge of the H-mode plasma (Fig. 2) as a function of its emitting source location in major radius, for a sequence of discrete frequency channels separated by 5 GHz for fundamental emission frequencies. Specific Intensity plots are shown for a perpendicular and oblique views at 10^o and 20^o from perpendicular. The emission at a fixed frequency, say 165 GHz (red) or 130 GHz (blue) moves to larger major radius in going from a perpendicular to 20^o oblique view because of the larger Doppler shift as the view goes from perpendicular to oblique. Also, the major radial resolution actually improves for the moderately oblique views compared to the perpendicular view. This is because there is a higher optical depth for the oblique views. This modeling used only one ray launched along the axis of the antenna so the effects due to the finite width of the antenna pattern are not included. To assess the effects of finite antenna pattern width on radial resolution, modeling was performed with multiple rays at each frequency with the rays filling the antenna pattern. A 15 cm diameter cylindrical antenna pattern with Gaussian beam width of 3.7 cm was used. These results are shown by the dashed lines at 130 GHz and 165 GHz in the plot for the 20^o oblique view. Including finite antenna pattern width degraded the radial resolution by about 50% at 20^o but had a negligible effect at 10^o and for the perpendicular view. With the antenna width included, the major radial resolution for the 20^o oblique view was no worse than for the

perpendicular view. However, ECE at a given frequency is received from a larger major radius as the view becomes more oblique and re-absorption of fundamental ECE by the Doppler shifted second harmonic occurs at larger major radius, reducing the major radial access for the oblique views.

Refraction effects for the oblique views were minimal, as shown in Fig. 9, which plots the ray trajectories projected onto a toroidal cross section at the plasma midplane. These rays were computed with non-relativistic ray tracing, but when relativistic ray tracing was included for sample cases the differences with the non-relativistic results were found to be negligible.

Emission at fundamental and second harmonic is insensitive to wall reflections for the perpendicular view, and for the moderately oblique views it is insensitive to wall reflections at the third harmonic as well, as shown in Fig. 10 for O-mode polarization. So a viewing dump would not be required for the oblique views.

Another potential issue for using a moderately oblique view for the measurement of T_e, is that the thermal emission measured by the oblique views might be polluted by non-thermal emission from an energetic electron tail, generated for example during LHCD. Figure 11 summarizes the plasma conditions for an ITER plasma with 30 MW of LHCD. Figure 11(a) and (b) show the electron density and temperature profiles, respectively. $T_e(0)$ = 30 keV and $n_e(0) = 7\text{x}10^{19}\text{m}^{-3}$. Fig. 11(c) shows a poloidal cross section of the magnetic equilibrium. For this case the vertical position of the ECE antenna lies well above plasma midplane. LHCD generates current off axis at r/a = 0.65. The electron distribution near the LHCD peak at r/a = 0.65 is shown in Fig. 11(d) was calculated with the CQL3D Fokker-Planck code [11]. The LHCD generates an energetic electron tail that

extends to 500 keV. Figure 12 shows ECE spectra simulated for the LHCD plasma. The ECE T_{rad} is plotted versus the emission frequency normalized to the fundamental cyclotron frequency on axis, $f/f_{ce}(0)$, where $f_{ce}(0) = 133$ GHz. The O-mode ECE spectra for the LHCD case are shown in Fig. 12(a). The ECE spectra for the Maxwellian electron distribution are indicated by the three solid blue lines, the thickest line being for the normal perpendicular view and the thinnest being for the view that is 20^o from perpendicular. For the LHCD plasma conditions it is possible to use fundamental O-mode ECE to measure $T_e(R)$ but absorption by the downshifted second harmonic does not allow T_e measurements beyond the plasma axis. The ECE spectra for the non-Maxwellian electron distribution with LHCD are indicated by the three dashed red lines, the thickest line being for the normal perpendicular view and the thinnest being for the view that is 20^o from perpendicular. The Maxwellian and non-Maxwellian spectra are almost identical. The X-mode ECE spectra for the LHCD case are shown in Fig. 12(b). Once again, the Maxwellian and non-Maxwellian spectra are almost identical. The ECE spectra are insensitive to the energetic electron tail driven by LHCD.

In summary, if the bulk of the electron velocity distribution remains Maxwellian, modeling results predict that the moderately oblique views could be used to measure $T_e(R)$, even if an energetic electron tail is present. In addition no viewing dump would be required to measure $T_e(R)$ with the moderately oblique views, refraction effects should be minimal and the radial resolution is expected be similar to the perpendicular view.

(c) If the electron energy distribution has a bulk distortion, can a two-temperature distribution be reconstructed with only two views, one perpendicular and one moderately oblique?

There is a clear benefit to having oblique views at two different angles. For example in the H-mode case, with a non-Maxwellian, two-temperature bulk (Fig. 3), the O-mode fundamental ECE spectra from the perpendicular and 10^o views were very similar reaching $T_{ECE} \sim 40$ keV, close to the 50 keV temperature component in the bulk. In contrast, the 20^o view measured a maximum $T_{ECE} \sim 25$ keV, the temperature of the rest of the energy distribution. However, by using O-mode and X-mode spectral measurements over several harmonics, it should be possible to reconstruct a two-temperature bulk distribution from only one oblique and one perpendicular view. For example, the ratio of T_{ECE} from the 10^o and the perpendicular views at the O-mode fundamental, is very different to the ratio between the same views at the X-mode third harmonic.

In summary, while a two-antenna system, one perpendicular and one moderately oblique, is probably sufficient to reconstruct a two-temperature bulk distribution, a three-antenna system, one perpendicular and two moderately oblique, is preferred.

III. PROPOSED MODIFICATION TO E9 PORT PLUG

Several implementations of oblique viewing antennas were considered for the E9 port plug. Initially a design was considered that used an oblique antenna similar to the one recently installed on JET [12] that has perpendicular, 10^o and 20^o oblique views enabled by series of mirrors at the front of the antenna. Figure 13(a) shows a design where a 10^o oblique antenna is added to the two perpendicular antennas. This implementation would

require an additional waveguide run and calibration source. Figure 13(b) shows a design where a 10^o oblique antenna replaces one of the two perpendicular antennas. A major concern for these designs is that they require a mirror at the front of the port plug that that can potentially suffer significant neutron and plasma damage. A better approach for ITER would probably be to rotate the last section of waveguide run as shown in Fig. 14. This design is for a 10^o oblique view, but oblique angles of at least 20^o are possible without a major redesign of the port plug. An additional consideration for the oblique views is that the X-mode and O-mode emission will be elliptically polarized. A quarter-wave plate will need to be introduced into the optical transmission system in order to avoid significant mixing of X-mode and O-mode polarized ECE [13].

IV. CONCLUSIONS AND RECOMMENDATIONS

A two-view antenna system, with one perpendicular and one moderately oblique view, is probably sufficient to reconstruct a two-temperature bulk distribution, however a three-view antenna system, with one perpendicular and two moderately oblique views, would be preferred. A detailed error propagation analysis should be conducted to determine the accuracy of a two-temperature bulk distribution measurement. The least expensive implementation of an oblique view at E9 port plug would be to rotate the last section of waveguide run. Oblique angles of at least 20^o are possible without a major redesign of the port plug. If due to budget constraints only one oblique view can be funded we recommend installing a 10^o view. If two oblique views can be funded we recommend installing 10^o and 20^o views.

Under the typical conditions reviewed, a perpendicular viewing antenna on ITER will be sensitive to electron kinetic energies less than 10 keV, a 10^o oblique viewing antenna

will be sensitive to energies in the range 5-20 keV and a 20^o oblique viewing antenna will be sensitive to energies in the range 20-70 keV. If the bulk of the electron distribution remains Maxwellian, a moderately oblique view could still be used to measure $T_e(R)$, even if an energetic electron tail is present. No viewing dump would be required to measure $T_e(R)$. Refraction effects should be minimal and the radial resolution of the moderately oblique view is expected to be similar to a perpendicular view.

Other diagnostics on ITER can provide valuable information on the electron bulk distribution. For example, residuals in the fits to laser Thomson scattering spectra and multi-color soft X-ray measurements can provide important additional information regarding the electron velocity distribution. In addition, recent advances in the analysis of strongly-linked plasma diagnostic data, including ECE data [14], need to be applied to measuring and understanding the electron distribution behavior at high T_e in ITER.

ACKNOWLEDGEMENTS

This work was supported by the United States Department of Energy contributions to the ITER project under contract DE-AC05-00OR-22725.

REFERENCES

1. G. TAYLOR, *et al.*, *Proc. 8th Joint Workshop on ECE and ECRH* (Gut Ising, Germany, 1992) ed. H. HARTFUSS, p. 277.
2. G. TAYLOR, *et al.*, *Proc. 9th Joint Workshop on ECE and ECRH* (Borrego Springs, USA, 1995) ed. J. LOHR (World Scientific, Singapore, 1995), p. 485.
3. E. DE LA LUNA, *et al.*, *Rev. Sci. Instrum,* **74**, 1414 (2003).
4. V. KRIVENSKI, *et al.*, *Fusion Eng. Des.* **53**, 23 (2001).
5. P. BURATTI and M. ZERBINI, *Rev. Sci. Instrum*. **66**, 4208 (1995).
6. C. SOZZI, *et al*, *Proc. 14th Joint Workshop on ECE and ECRH*, (Santorini, Greece, May 2006) ed. Avrilios Lazaros (Heliotopos Conferences Ltd., Athens, Greece, 2006, ISBN: 960-89228-2-8) p. 157.
7. A.SIMONETTO, *et al.*, *Proc. 14th Joint Workshop on ECE and ECRH*, (Santorini, Greece, May 2006) ed. Avrilios Lazaros (Heliotopos Conferences Ltd., Athens, Greece, 2006, ISBN: 960-89228-2-8) p. 238.
8. G. VAYAKIS, et al, "ECE Diagnostics for RTO/RC ITER", *Fusion Eng. Des*. **53**, 221 (2001).
9. A.P. SMIRNOV AND R.W. HARVEY, *Bull. Amer. Phys. Soc.* **40,** 1837, abstract 8P35, (1995).
10. R.W. HARVEY, M.R. O'BRIEN, M.G. MCCOY, AND G.D. KERBEL, *7th Joint Workshop and IAEA TCM on Electron Cylotron Emission and Electron Cyclotron Resonance Heating*, Hefei, China (1989); R.W. HARVEY, M.R. O'BRIEN, V.ROZHDESTVESKY, T. C. LUCE, M. G. MCCOY AND G. D. KERBEL, *Phys. Fluids B* **5**, 446 (1993).

11. R.W. HARVEY AND M.G. MCCOY, *Proceedings of the IAEA Technical Committee on Advances in Simulation and Modeling of Thermonuclear Plasmas*, Montreal, Quebec (International Atomic Energy Agency, Vienna, 1993), p. 489; USDOC NTIS Doc. No. DE93002962.

12. C. SOZZI et al., *Fusion Eng. Des.* **74**, 691 (2005).

13. O. TUDUSCO et al., Proc. 28th EPS Conf. on Contr. Fusion and Plasma Phys. (Funchal, June 2001) ECA Vol. **25A** (2001) pp. 1221-1224

14. A. DINKLAGE, et al., Fusion Sci. Technol. **41**, 355 (2004).

FIGURE CAPTIONS

Figure 1

Example of the disagreement between $T_{ECE}(0)$ and $T_{TS}(0)$ measurements observed in TFTR. The disagreement was similar in JET. $T_{ECE}(0)$ being about 20% higher than $T_{TS}(0)$ at $T_{ECE}(0)$ = 10 keV.

Figure 2

ITER H-mode plasma parameters used to model ECE. (a) The electron density profile, (b) the electron temperature profile, (c) poloidal cross section of the plasma magnetic equilibrium and (d) the electron energy distribution on axis for the Maxwellian (blue solid line) and non-Maxwellian (red dashed line) cases. The non-Maxwellian distribution has the electron temperature increased by a factor of two between 0.75 and 1.5 times the electron thermal velocity.

Figure 3

Simulated ECE spectra for the H-mode plasma shown in Fig. 2. (a) O-mode and (b) X-mode ECE spectra plotted versus emission frequency normalized to the fundamental cyclotron frequency on axis ($f_{ce}(0)$ = 149 GHz). Emission spectra are shown for an ECE antenna pointing with its axis 0^o, 10^o and 20^o to perpendicular to the outer plasma magnetic flux surface (as illustrated in Fig. 3(c)). ECE spectra are plotted for a Maxwellian electron distribution (solid blue lines) and the non-Maxwellian distribution shown in Fig. 2(d) (red dashed lines).

Figure 4

O-mode polarized emission flux measured at the edge of the H-mode plasma of Fig. 2 plotted as a function of emission frequency and electron energy of the emission source.

The plots show the electron energies contributing to the measured flux. Spectra are shown for an ECE antenna pointing at a Maxwellian electron distribution (blue solid lines in Fig. 2(d)) with its axis (a) 0^o, (c) 10^o and (e) 20^o from perpendicular to the outer plasma magnetic flux surface. O-Mode polarized spectra are also shown for an ECE antenna pointing at a non-Maxwellian electron distribution (red dashed lines in Fig. 2(d)) measured by an ECE antenna pointing with its axis (a) 0^o, (c) 10^o and (e) 20^o to perpendicular.

Figure 5

X-mode polarized emission flux measured at the edge of the H-mode plasma of Fig. 2 plotted as a function of emission frequency and electron energy of the emission source. The plots show the electron energies contributing to the measured flux. Spectra are shown for an ECE antenna pointing at a Maxwellian electron distribution (blue solid lines in Fig. 2(d)) with its axis (a) 0^o, (c) 10^o and (e) 20^o from perpendicular to the outer plasma magnetic flux surface. X-Mode polarized spectra are also shown for an ECE antenna pointing at a non-Maxwellian electron distribution (red dashed lines in Fig. 2(d)) measured by an ECE antenna pointing with its axis (a) 0^o, (c) 10^o and (e) 20^o to perpendicular.

Figure 6

O-mode fundamental and X-mode second harmonic ECE emission flux spectra measured at the edge of the H-mode plasma of Fig. 2 with a Maxwellian electron distribution (the blue solid lines in Fig. 2(d)). O-mode fundamental spectra measured at (a) 0^o, (b) 10^o and (c) 20^o to perpendicular and X-mode second harmonic spectra measured at (d) 0^o, (e) 10^o and (f) 20^o to perpendicular. The electron energy range contributing to the measured emission flux increases from 0-15 keV at 0^o to 30-80 keV at 20^o.

Figure 7

O-mode fundamental and X-mode second harmonic ECE emission flux spectra measured at the edge of the H-mode plasma of Fig. 2 with the non-Maxwellian electron distribution (the red dashed lines in Fig. 2(d). O-mode fundamental spectra measured at (a) 0^o, (b) 10^o and (c) 20^o to perpendicular and X-mode second harmonic spectra measured at (d) 0^o, (e) 10^o and (f) 20^o to perpendicular.

Figure 8

Specific emission intensity versus major radius for 5 GHz separated ECE channels using O-mode fundamental emission from the H-mode plasma with a Maxwellian electron distribution (Fig. 2). Specific intensity data is plotted for three cases with the ECE antenna axis pointing at 0^o, 10^o and 20^o to perpendicular. Results shown by the solid curves are calculated for a single ray on the antenna axis. The dashed curves show the effect of using a finite 15 cm wide beam with a Gaussian width of 3.7 cm. Finite beam width broadens the radial spatial resolution the most for the 20^o to perpendicular view, but the spatial resolution is about the same as for the perpendicular view.

Figure 9

Ray trajectories for the 0^o, 10^o and 20^o antennas projected onto the plasma toroidal midplane. Refraction is minimal for the oblique views.

Figure 10

Comparison of O-mode ECE spectra plotted versus frequency normalized to the fundamental electron cyclotron frequency at the magnetic axis ($f_{ce}(0)$ = 149 GHz) for the Maxwellian H-mode plasma (Fig. 2). Spectra are shown with wall reflections included (black solid line) and without reflections (dashed red line). No viewing dump is needed for the oblique views in order to measure $T_e(R)$ using the fundamental O-mode ECE.

Figure 11

ITER LHCD plasma parameters used to model ECE. (a) The electron density profile, (b) the electron temperature profile, (c) poloidal cross section of the plasma magnetic equilibrium and (d) the electron energy distribution at r/a = 0.65, the radial location where the LHCD current density peaks. 30 MW of LHCD was used for this case.

Figure 12

Simulated ECE spectra for the LHCD plasma parameters shown in Fig. 11. (a) O-mode and (b) X-mode ECE spectra plotted versus emission frequency normalized to the fundamental cyclotron frequency on axis ($f_{ce}(0)$ = 133 GHz). Emission spectra are shown for an ECE antenna pointing with its axis 0^o, 10^o and 20^o from perpendicular to the outer plasma magnetic flux surface. ECE spectra are plotted for a Maxwellian electron distribution without LHCD (blue solid line) and with the Lower Hybrid driven electron tail included (red dashed line). The measured ECE spectra at 0^o, 10^o and 20^o from perpendicular are insensitive the energetic electron tail.

Figure 13

(a) 3-D rendered drawing of the ITER E9 port plug with one 10^{o} antenna added to the two perpendicular antennas and (b) with one 10^{o} antenna replacing one of the two perpendicular antennas.

Figure 14

(a) 3-D rendered drawing of the front of the modified E9 port plug, showing 10^{o} to perpendicular oblique view, made possible by rotating one of the two perpendicular viewing antennas in the original E9 port plug design. Oblique angles at least 20^{o} to perpendicular are possible without major redesign of the E9 port port plug. (b) top view, (c) side view and (d) front view drawings of 10^{o} oblique ECE antenna.

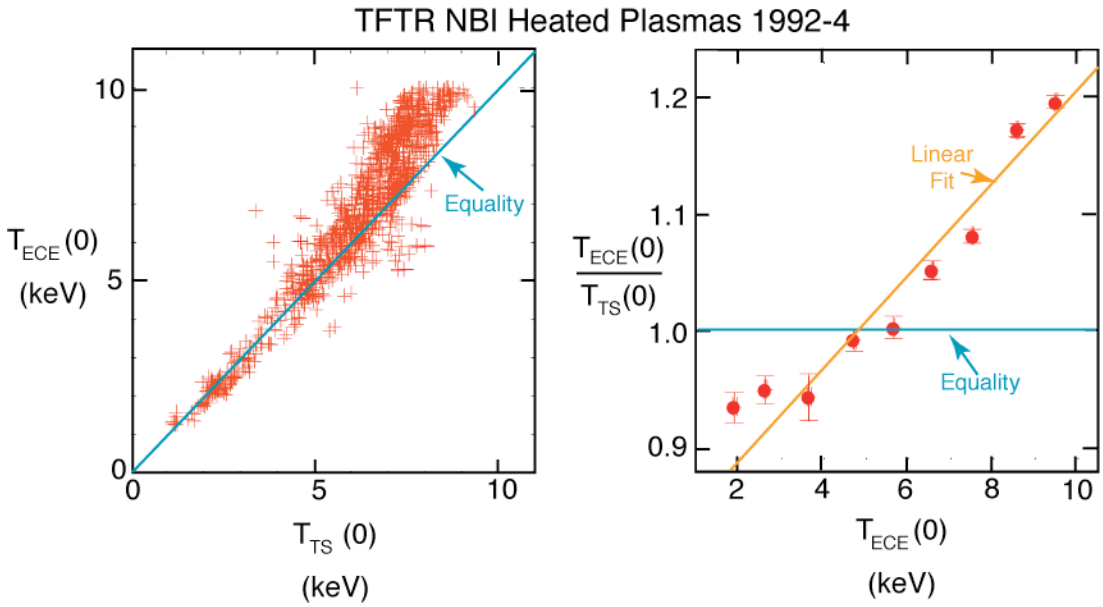
TFTR NBI Heated Plasmas 1992-4
$T_{ECE}(0)$ (keV)
$T_{TS}(0)$ (keV)
Equality
$\frac{T_{ECE}(0)}{T_{TS}(0)}$
$T_{ECE}(0)$ (keV)
Linear Fit
Equality

Figure 1

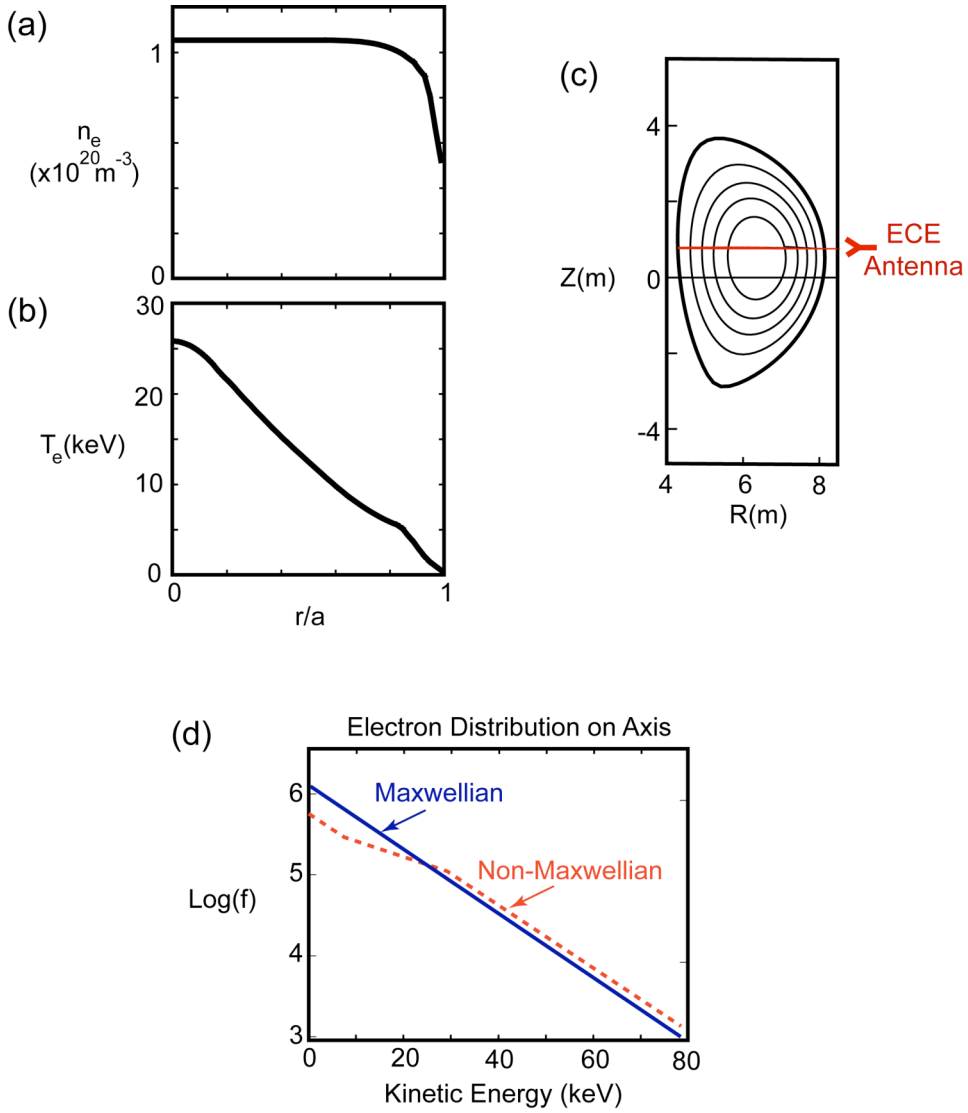
(a)
1
n_e
($x10^{20}$ m^{-3})
0
(b)
30
20
T_e(keV)
10
0
0
1
r/a
(c)
4
Z(m)
0
-4
4
6
8
R(m)
ECE
Antenna
(d)
Electron Distribution on Axis
Maxwellian
Non-Maxwellian
Log(f)
6
5
4
3
0
20
40
60
80
Kinetic Energy (keV)

Figure 2

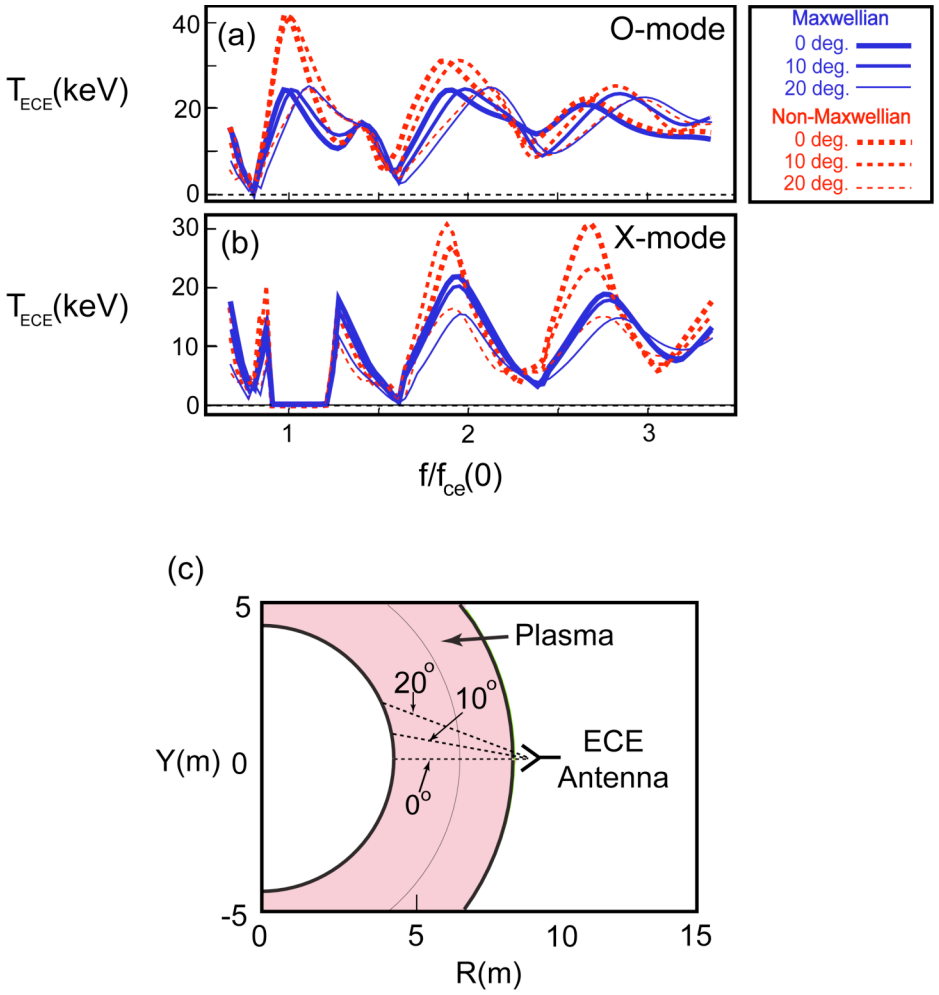
(a)
O-mode
(b)
X-mode
T_{ECE}(keV)
T_{ECE}(keV)
40
20
0
30
20
10
0
1
2
3
f/f_{ce}(0)
Maxwellian
0 deg.
10 deg.
20 deg.
Non-Maxwellian
0 deg.
10 deg.
20 deg.
(c)
5
Y(m) 0
-5
0
5
10
15
R(m)
Plasma
20°
10°
0°
ECE
Antenna

Figure 3

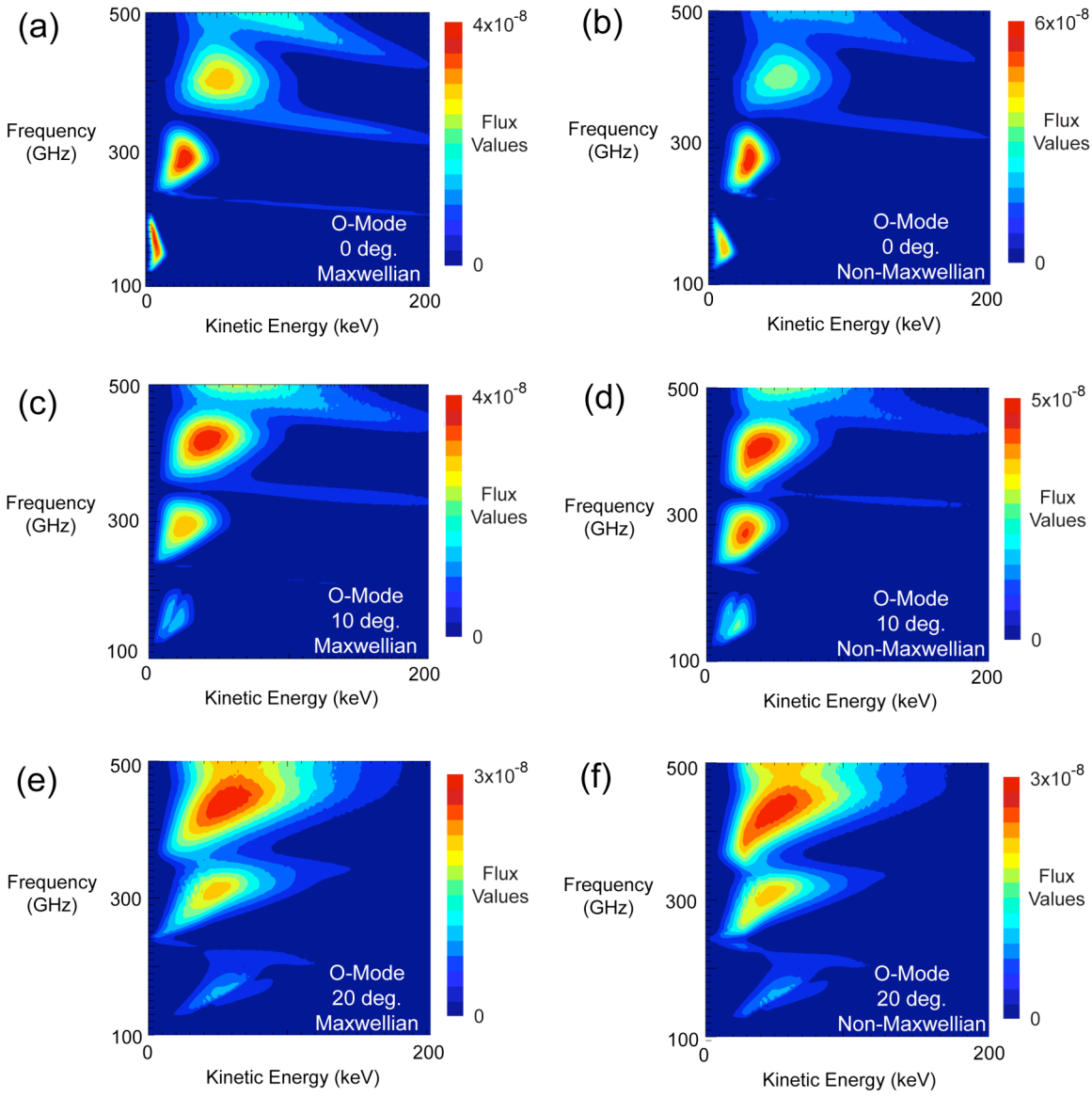
(a)
O-Mode
0 deg.
Maxwellian
(b)
O-Mode
0 deg.
Non-Maxwellian
(c)
O-Mode
10 deg.
Maxwellian
(d)
O-Mode
10 deg.
Non-Maxwellian
(e)
O-Mode
20 deg.
Maxwellian
(f)
O-Mode
20 deg.
Non-Maxwellian
Frequency (GHz)
Kinetic Energy (keV)
Flux Values
500
300
100
0
200
4x10-8
6x10-8
5x10-8
3x10-8

Figure 4

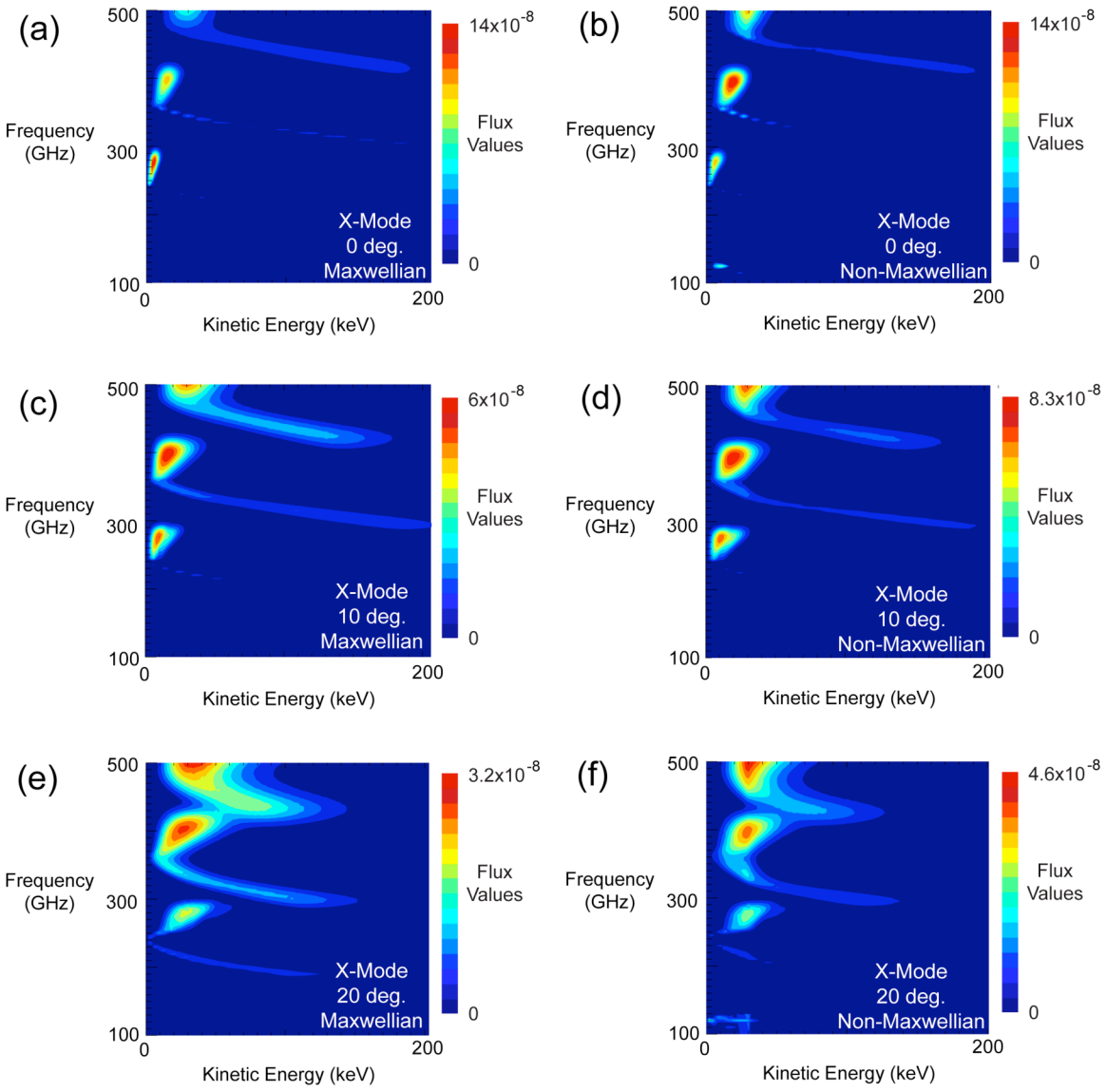
(a)
Frequency (GHz)
500
300
100
0
200
Kinetic Energy (keV)
X-Mode
0 deg.
Maxwellian
14x10-8
Flux Values
0
(b)
Frequency (GHz)
500
300
100
0
200
Kinetic Energy (keV)
X-Mode
0 deg.
Non-Maxwellian
14x10-8
Flux Values
0
(c)
Frequency (GHz)
500
300
100
0
200
Kinetic Energy (keV)
X-Mode
10 deg.
Maxwellian
6x10-8
Flux Values
0
(d)
Frequency (GHz)
500
300
100
0
200
Kinetic Energy (keV)
X-Mode
10 deg.
Non-Maxwellian
8.3x10-8
Flux Values
0
(e)
Frequency (GHz)
500
300
100
0
200
Kinetic Energy (keV)
X-Mode
20 deg.
Maxwellian
3.2x10-8
Flux Values
0
(f)
Frequency (GHz)
500
300
100
0
200
Kinetic Energy (keV)
X-Mode
20 deg.
Non-Maxwellian
4.6x10-8
Flux Values
0

Figure 5

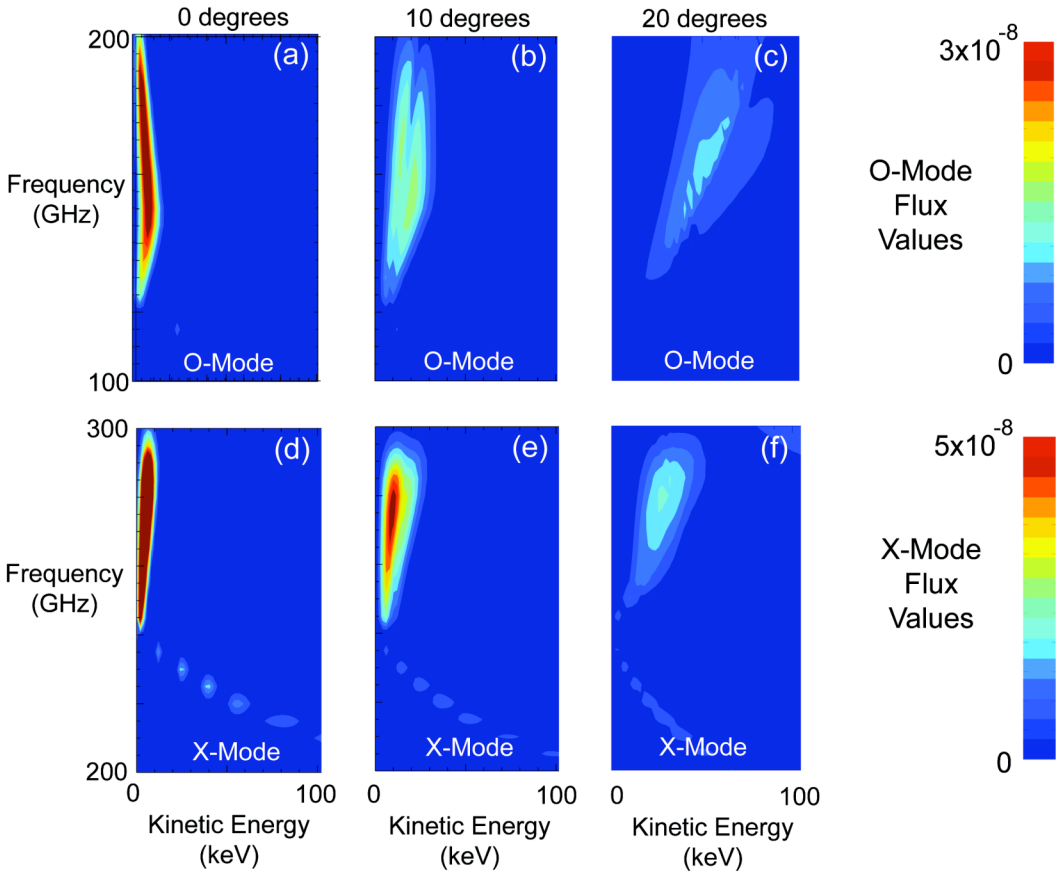
0 degrees
10 degrees
20 degrees
(a)
(b)
(c)
(d)
(e)
(f)
O-Mode
X-Mode
Frequency (GHz)
200
100
300
0
100
Kinetic Energy (keV)
3x10-8
O-Mode Flux Values
5x10-8
X-Mode Flux Values

Figure 6

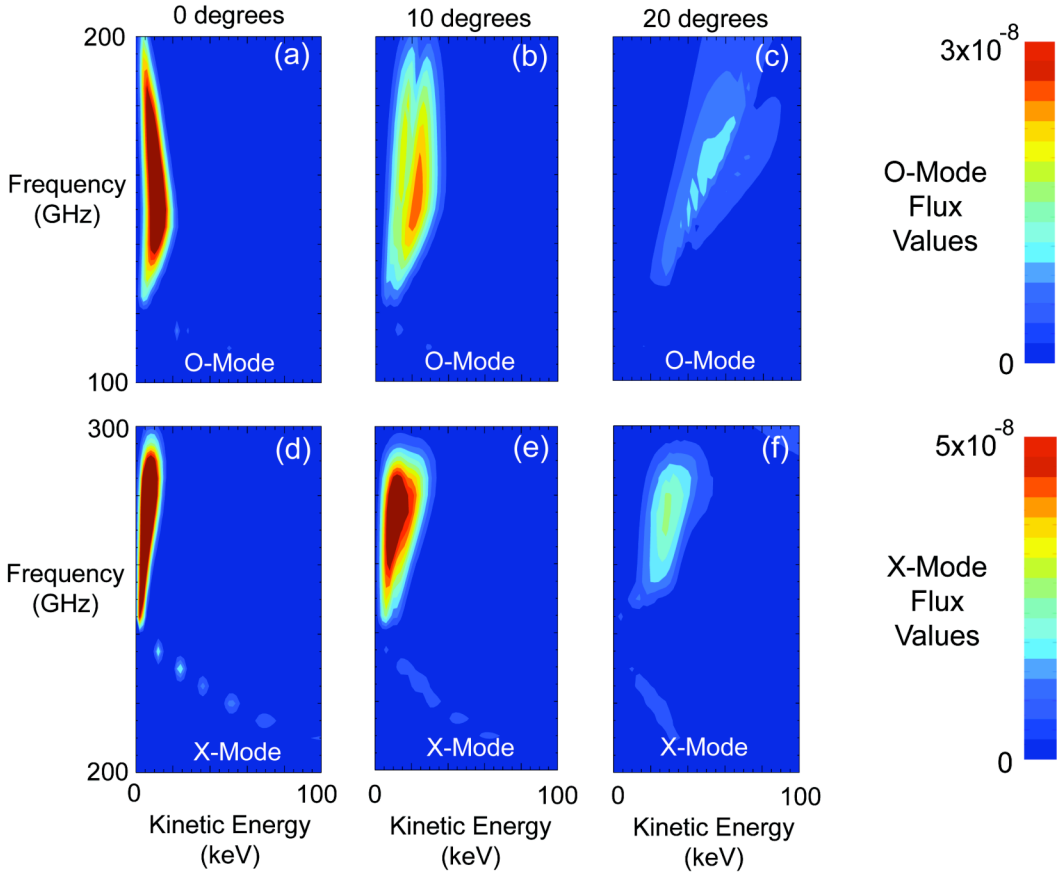
0 degrees
10 degrees
20 degrees
200
100
300
200
(a)
(b)
(c)
(d)
(e)
(f)
O-Mode
X-Mode
Frequency (GHz)
Kinetic Energy (keV)
0
100
3x10-8
5x10-8
O-Mode Flux Values
X-Mode Flux Values

Figure 7

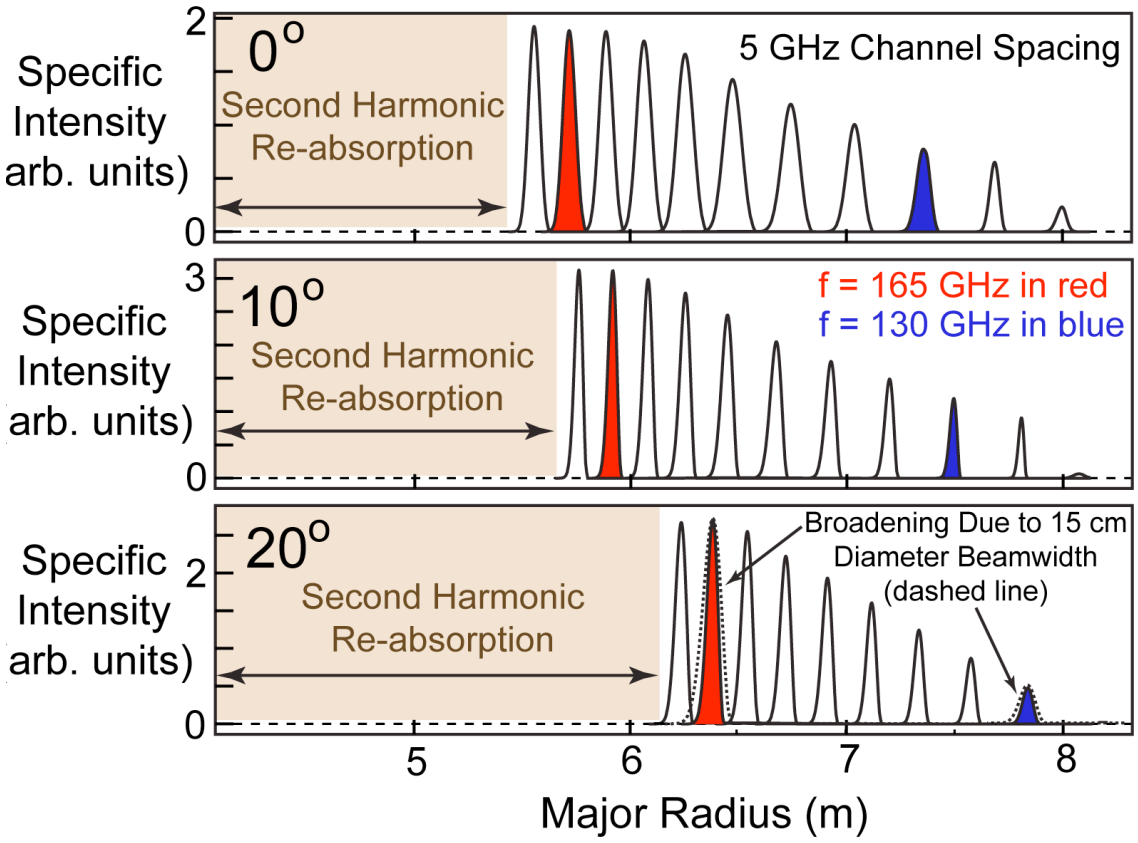
Specific Intensity arb. units)
2
0
0°
Second Harmonic Re-absorption
5 GHz Channel Spacing
Specific Intensity arb. units)
3
0
10°
Second Harmonic Re-absorption
f = 165 GHz in red
f = 130 GHz in blue
Specific Intensity arb. units)
2
0
20°
Second Harmonic Re-absorption
Broadening Due to 15 cm Diameter Beamwidth (dashed line)
5
6
7
8
Major Radius (m)

Figure 8

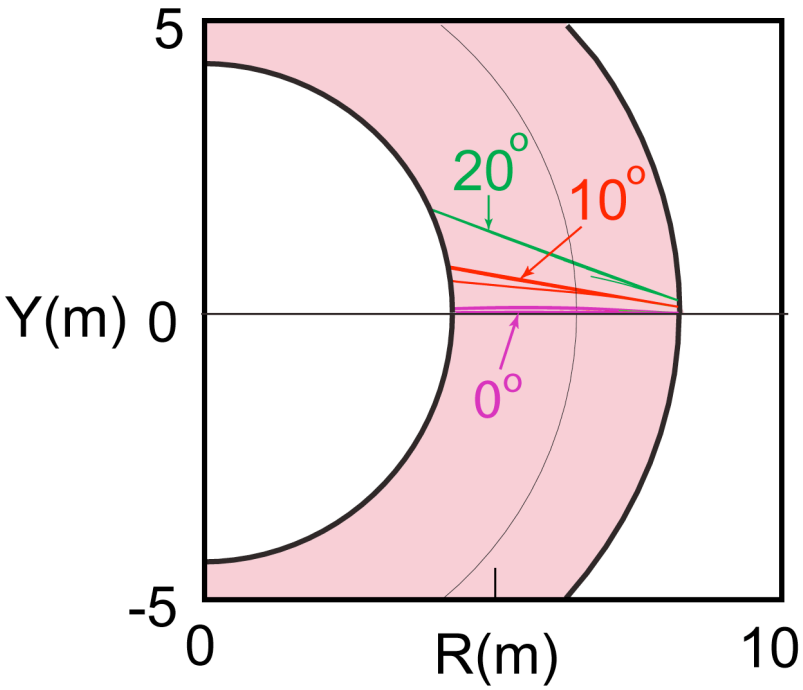

Figure 9

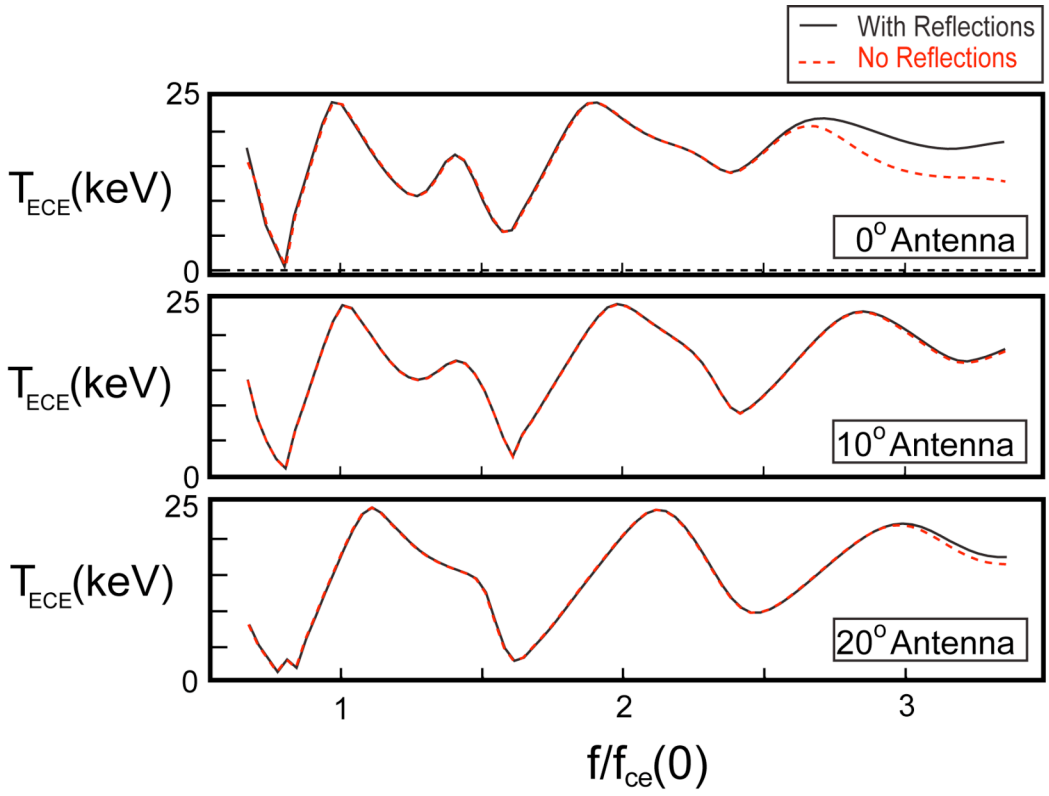
With Reflections
No Reflections
25
0
T_{ECE}(keV)
0° Antenna
10° Antenna
20° Antenna
1
2
3
$f/f_{ce}(0)$

Figure 10

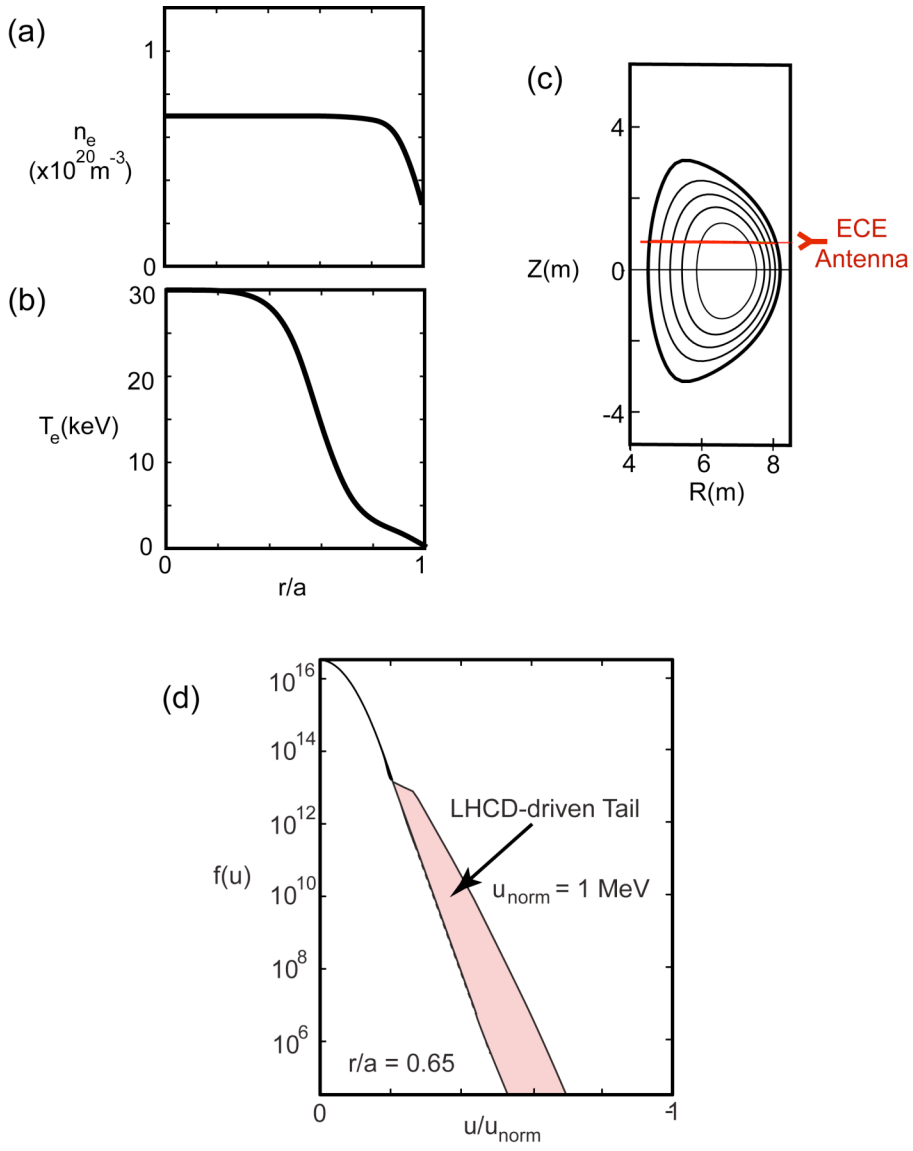
(a)
1
n_e
(x10^{20} m^{-3})
0
(b)
30
20
T_e(keV)
10
0
0
1
r/a
(c)
4
Z(m)
0
-4
4
6
8
R(m)
ECE
Antenna
(d)
10^{16}
10^{14}
10^{12}
f(u)
10^{10}
10^{8}
10^{6}
LHCD-driven Tail
u_{norm} = 1 MeV
r/a = 0.65
0
u/u_{norm}

Figure 11

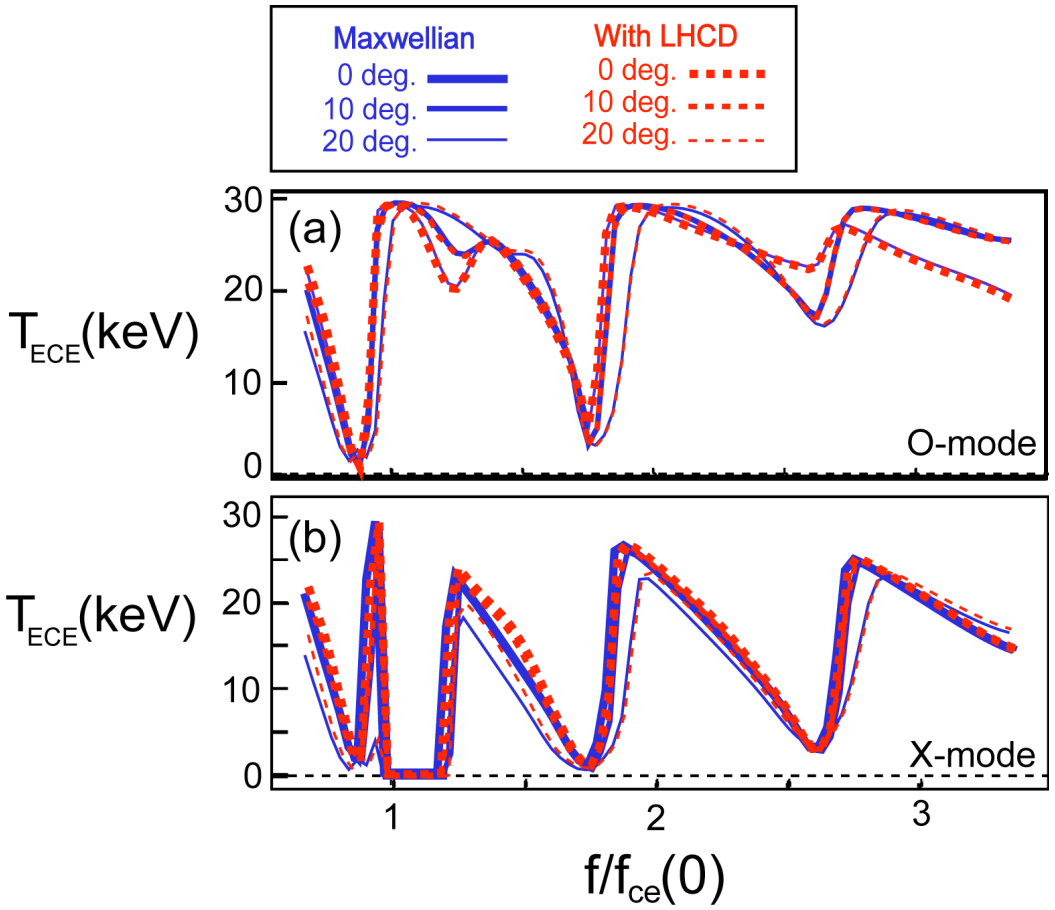
Maxwellian
0 deg.
10 deg.
20 deg.
With LHCD
0 deg.
10 deg.
20 deg.
(a)
O-mode
(b)
X-mode
T_{ECE}(keV)
T_{ECE}(keV)
30
20
10
0
1
2
3
$f/f_{ce}(0)$

Figure 12

(a)

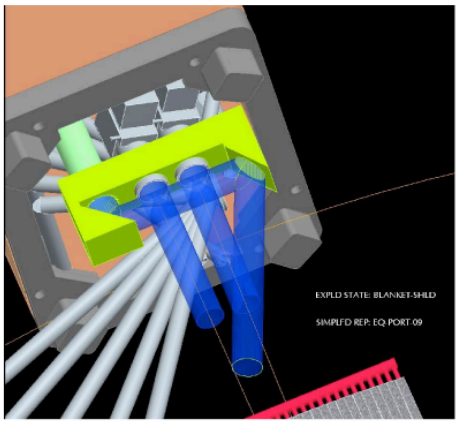

(b)

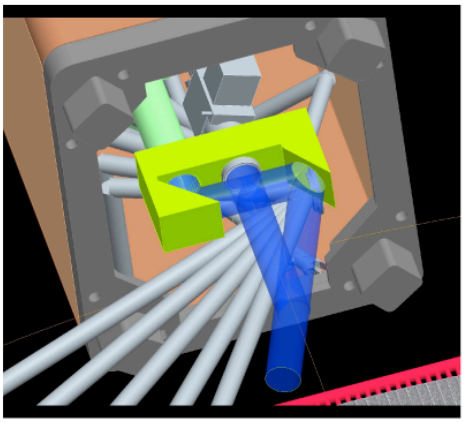

Figure 13

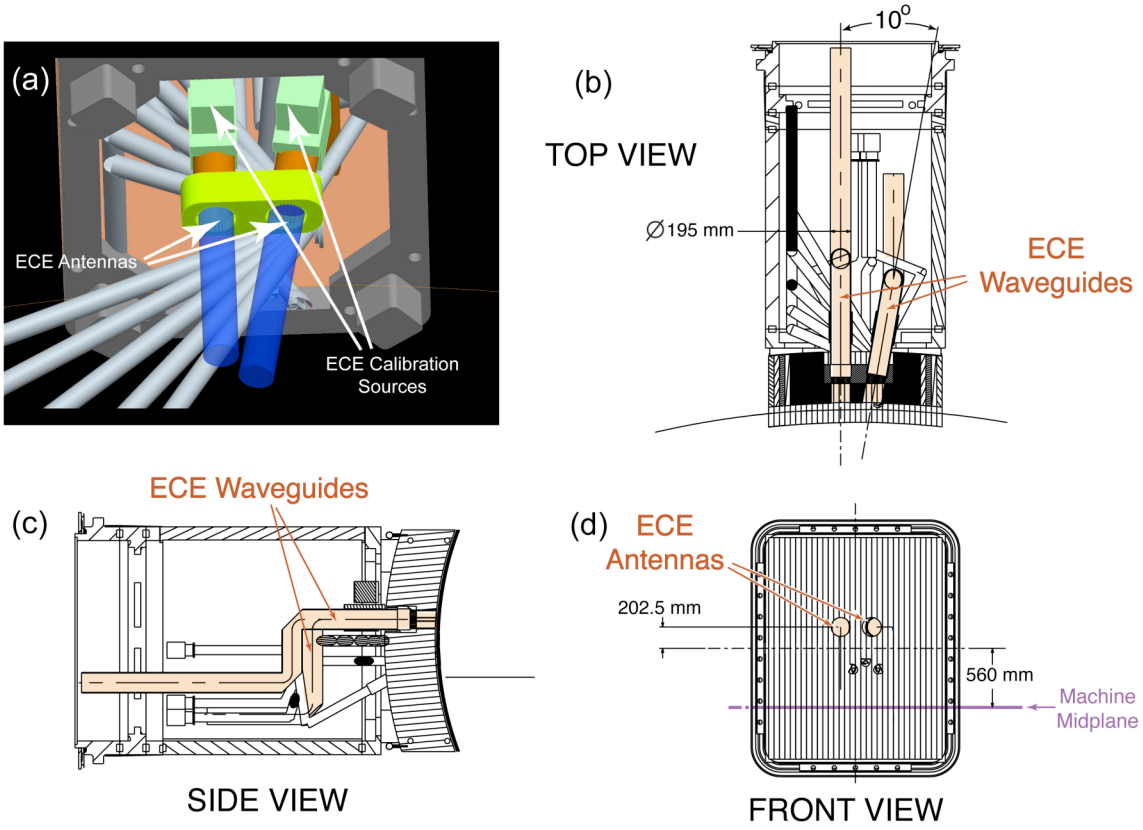
(a)
ECE Antennas
ECE Calibration Sources
(b)
TOP VIEW
10°
Ø195 mm
ECE Waveguides
(c)
ECE Waveguides
SIDE VIEW
(d)
ECE Antennas
202.5 mm
560 mm
Machine Midplane
FRONT VIEW

Figure 14

The Princeton Plasma Physics Laboratory is operated
by Princeton University under contract
with the U.S. Department of Energy.

Information Services
Princeton Plasma Physics Laboratory
P.O. Box 451
Princeton, NJ 08543

Phone: 609-243-2750
Fax: 609-243-2751
e-mail: pppl_info@pppl.gov
Internet Address: http://www.pppl.gov